Journal of Alloys and Compounds 507 (2010) 236–244

Contents lists available at ScienceDirect

Journal of Alloys and Compounds

journal homepage: www.elsevier.com/locate/jallcom

Effect of strengthening mechanisms on cold workability and instantaneous strain hardening behavior during grain refinement of AA 6061-10 wt.% TiO_2 composite prepared by mechanical alloying

S. Sivasankaran[a], K. Sivaprasad[b], R. Narayanasamy[a,*], Vijay Kumar Iyer[c]

[a] Department of Production Engineering, National Institute of Technology, Tanjore Main Road, Tiruchirappalli 620015, Tamil Nadu, India
[b] Department of Metallurgical and Materials Engineering, National Institute of Technology, Tiruchirappalli 620015, India
[c] Powder Metallurgy Shop, Heavy Alloy Penetrator Project, Tiruchirappalli 620025, India

ARTICLE INFO

Article history:
Received 2 July 2010
Accepted 24 July 2010
Available online 4 August 2010

Keywords:
Mechanical alloying
Cold workability
Strengthening mechanism
Strain hardening

ABSTRACT

The mechanical alloying (MA) of AA 6061 alloy reinforced with 10 wt.% fine anatase-titania composites powder milled with different timings (1, 5, 10, 20, 30, and 40 h) was cold consolidated and sintered. The main purpose of this study is to investigate the effect of microstructure and the various strengthening mechanisms such as solid solution, grain size, precipitate, dislocation and dispersion strengthening during grain refinement of AA 6061-10 wt.% TiO_2 composite via MA on cold working and strain hardening behavior. The sintered composite preforms were characterized by X-ray diffraction, scanning electron microscope, and transmission electron microscope. The strengthening mechanisms were estimated by using simplified models available in the literatures. The evaluation of cold deformation behavior under triaxial stress condition through room temperature cold-upsetting tests (incremental loads) was studied by correlating the strengthening mechanisms. Among the developed strengthening mechanisms the grain size and dislocation strengthening mechanisms diminished the deformation capacity of the composites. The strain hardening behavior was also examined by proposing instantaneous strain hardening index (n_i). The value of maximum instantaneous strain hardening index for ultrafine-grained composite was to be about twice that of coarse-grained composite at lower true axial strain value. Also, the coarse grained 5 h composite was observed to be the best one as it exhibited a better strain hardening or deformation behavior.

1. Introduction

Ultrafine-grained (UFG), fine-grained (FG) and nanocrystalline (NC) materials are increasingly being studied owing to their improved mechanical properties. Bulk UFG or NC metals, alloys and composites are commonly produced by high-energy ball milling [1], equal channel angular pressing [2], and high pressure torsion [3]; which are under the category of severe plastic deformation (SPD). During SPD, very large plastic strains have been introduced which led to grain refinement in coarse-grained (CG) powder. Grain refinement plays a vital role in Al-alloy based composites. Apart from cast Al-alloy based composites; grain refinement has several benefits via mechanical alloying (MA) followed consolidation by conventional powder metallurgy (P/M) process; which improves the mechanical properties, distribution of second phase particles, better strength and fatigue life.

Structural applications of Al-alloy based composites at high or moderate temperatures require a fine, homogeneous and stable distribution of particles to guarantee the dispersion hardening up to the temperature of use. Although particle dispersion can be obtained by conventional ingot metallurgy, problems as formation of coarse intermetallic particles and segregation during the ingot solidification usually takes place [4,5]. These problems can be overcome by using P/M and more specifically MA as processing route [3,6–8]. MA is a solid-state processing that enables refinement of the microstructure, homogenization and extension of solid solubility limits [9–11]. The possibility of higher solubility could be interesting to enhance precipitation of equilibrium phases in the heat treatable Al-alloys via MA. The highest strength Al-alloys with applications in the aircraft and automated industry are those of 6XXX series; which have a good formability and heat treatable alloy. Also, to facilitate the prevention of reinforcement clusters or agglomerates on the matrix, especially in the case of small size reinforcement particles, MA is one of the P/M processes that produces uniform dispersion of the reinforcement particles in the matrix.

---

* Corresponding author. Tel.: +91 431 250 3504; fax: +91 431 250 0133.
E-mail addresses: sivasankarangs1979@gmail.com (S. Sivasankaran), ksp@nitt.edu (K. Sivaprasad), narayan@nitt.edu, narayan10455@yahoo.co.in (R. Narayanasamy), yajiv29@yahoo.com (V.K. Iyer).

0925-8388/$ – see front matter © 2010 Elsevier B.V. All rights reserved.
doi:10.1016/j.jallcom.2010.07.168

Generally, the reinforcement clusters on the matrix has occurred when the particle size of matrix-to-reinforcement ratio exceeds one, which deteriorates the mechanical properties. This problem is encountered in conventional P/M process [12], however, this can be avoided in MA [13,14].

Numerous investigations have been carried out regarding strain hardening behavior through tensile tests during grain refinement [15–17]. In fact, the uniaxial tensile test would not be able to sustain a uniform tensile deformation at ambient temperature for more than a couple of percent of plastic strain especially in refined grain materials. Hence, compression tests (here, cold-upsetting) are needed to provide a direct evaluation of the strain hardening response as a function of true strain because the compressive behavior is not strongly influenced by superfluous factors such as surface or internal blemish [18]. Further, limited studies are reported on the strain hardening behavior of materials through compression tests [19–21]. But, there is no work on cold workability and strain hardening behavior under cold-upsetting (triaxial stress condition) of AA 6061-10 wt.% TiO_2 composite during grain refinement processed by MA.

Workability is a term used to evaluate the capacity of a material to withstand the induced internal stresses of forming prior to the splitting of material occurs. The cold workability and the strain hardening behavior of porous P/M composites under uniaxial, plane and triaxial conditions were elaborately analysed and discussed in the previous works by Narayanasamy et al. [22–25]. Their results have shown that the workability behavior of metals/alloys/composites of P/M components depends on the aspect ratio, the preform geometry, the particle size and the percentage of reinforcement for the composites, the die geometry, the lubricants, and the compacting load. However, this is not the aim of the present work, instead, to study the effect of grain refinement on the cold workability and its strain hardening behavior of AA 6061-10 wt.% TiO_2 composite via MA. According to the findings of Narayanasamy et al. [22–25], porous P/M material during cold working not only experiences the usual strain hardening but also experiences 'geometrical work-hardening (GWH)' (due to a continued increase in density which leads to the enhancement in area of the cross-section) and 'matrix work-hardening (MWH)' (due to continuous increase in strength of the matrix with increase in strain). In general, GWH mainly depends on stress required for closing of pores during compressive plastic deformation [22–25].

As reported in previous work [13], a commercial AA 6061 Al-alloy based composite was produced by MA with titania addition. The main objective was to produce a dispersion-hardened alloy by TiO_2 particles [13]. The precursor powders produced by MA were cold compacted and then sintered in different temperatures. The consolidated samples in the as-sintered condition were characterized. Results showed that MA increased the mechanical properties of the AA 6061 Al-alloys and the respective composites when compared to the commercial one. This was attributed to contributions of various strengthening mechanisms resulting from the milling such as grain size refinement to nanometric scale and increase in dislocation density due to severe deformation caused by the MA process. The strengthening mechanism was not carried out in the previous work. Hence, the main objectives of the present work are threefold. Firstly to investigate the dominant strengthening mechanisms and suggest a strength model for AA 6061 reinforced with 10 wt.% TiO_2 (higher percentage, ≈45 matrix-to-reinforcement particle size ratio) particles with different milling time in as-sintered condition. The strengthening mechanism includes the solid solution, dispersoid, precipitate, forest dislocation and grain size strengthening. Secondly to study the effect of strengthening mechanisms on the cold workability during grain refinement and at last its strain hardening behavior by proposing instantaneous strain hardening index (n_i) under triaxial stress state condition.

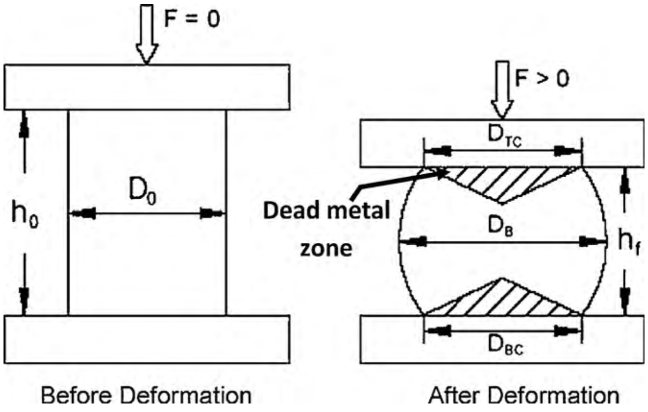

Fig. 1. The upset forging test-before and after deformation.

2. Experimental details

As reported elsewhere [13], powder of an AA 6061 based alloy with composition 99.68Al–0.68Si–0.7Fe–0.275Cu–0.15Mn–1Mg–0.195Cr–0.25Zn–0.15Ti (wt.%) with addition of 10 wt.% TiO_2 (anatase form with tetragonal structure, <1 μm average particle size, 3.84 g/cm^3 density) was produced by MA using pure elemental powders as starting materials. MA was carried out using a planetary ball mill (Insmart systems, Hyderabad, India) in toluene at 280 rpm and a ball-to-powder ratio of 10:1 using a hardened stainless steel media in different milling times, 1, 5, 10, 20, 30, and 40 h. Further details of milling, powder morphology and structural evaluation of the milled powders were reported in [13,14]. The precursor powders obtained by MA were consolidated with diameter 30 mm by cold compaction at 350 MPa (machined to get aspect ratio 0.375 related to P/M components) followed degassing at 623 K (45 min) and then sintering (N_2 atmosphere with mass flow rate of 6 m^3 per hour) at 848 K for 90 min in a mechanical pusher furnace as applicable to P/M industries. Phase identification and structural properties of the sintered composites were characterized by X-ray diffraction (XRD) using Cu-Kα radiation (1.5406 Å) in a D/MAX ULTIMA III diffractometer (Rigaku Corporation, Japan) operating at 30 mA and 40 kV. From the XRD peak profile, instrumental broadening and $K_{\alpha 2}$ components were subtracted and then the crystallite size was estimated using Williamson and Hall method [26]. Lattice parameter of the matrix was calculated from the first five peaks using Cullity method [27].

The microstructure of the as-sintered composites was examined by HITACHI S 3000H scanning electron microscope with back scattered electron image (SEM/BSEI) and PHILIPS CM12 transmission electron microscope (TEM). Hardness was measured using PC based Ratnakar Vickers tester at a load of 1 kg. Averages of at least 15 measurements were taken for each hardness value. The resulting sintered composites were subjected to incremental compressive load (cold-upsetting) of 5 kN between two flat mirror finished open dies on a hydraulic press (100 tones capacity). The initial diameter (D_0), height (h_0) and density (ρ_0) were measured and recorded. The deformation was carried out until the appearance of the first visible crack on the free surface. After each interval of loading, dimensional changes in the specimen such as height after deformation (h_f), top contact diameter (D_{TC}), bottom contact diameter (D_{BC}), bulged diameter (D_B) and density of the preform (ρ_f) were measured. At least five readings were taken and the average was used for investigation. The schematic diagram showing the various parameters measured before and after deformation is provided in Fig. 1. The density (average of five readings) of cold-upset preforms after every incremental loading was measured using Archimedes principle.

3. Results and discussion

3.1. X-ray diffraction and TEM analysis

Fig. 2 shows the XRD patterns of AA 6061-10 wt.% TiO_2 composite to different milling times after sintering. The sample consists of mainly α-Al, TiO_2 and Al_2O_3 phases. The observed Al_2O_3 phase as a precipitate was expected to form due to the oxidation of matrix of α-Al phase during sintering; which was of unknown type as given by the JCPDS data base (31-0026). Though the samples were sintered at N_2 atmosphere in mechanical pusher furnace, the presence

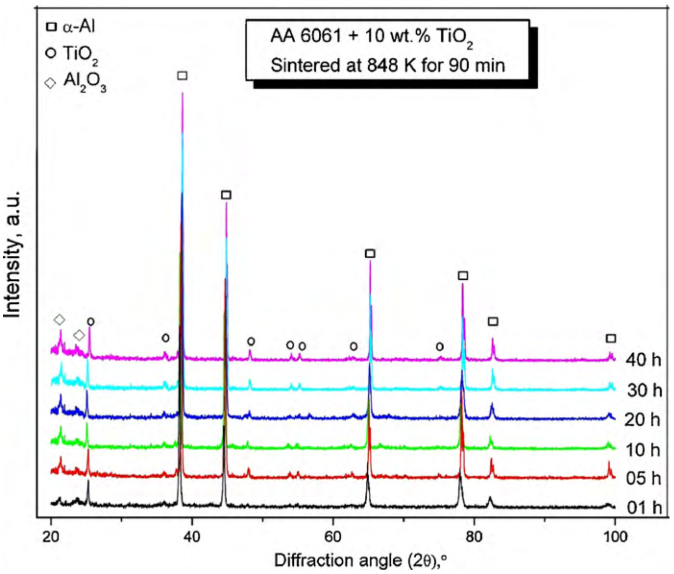

Fig. 2. XRD patterns of sintered AA 6061-10 wt.% TiO_2 composites as function of milling time.

Table 1
Phase evaluation of AA 6061-10 wt.% TiO_2 composites after sintering at 848 K for 90 min.

Milling time, h	Phase formation after sintering at 848 K for 90 min (crystallite size, nm)
1	α-Al (1602) + TiO_2 (45) + Al_2O_3 (38)
5	α-Al (792) + TiO_2 (44) + Al_2O_3 (38)
10	α-Al (545) + TiO_2 (41) + Al_2O_3 (38)
20	α-Al (374) + TiO_2 (40) + Al_2O_3 (38)
30	α-Al (304) + TiO_2 (40) + Al_2O_3 (38)
40	α-Al (292) + TiO_2 (39) + Al_2O_3 (38)

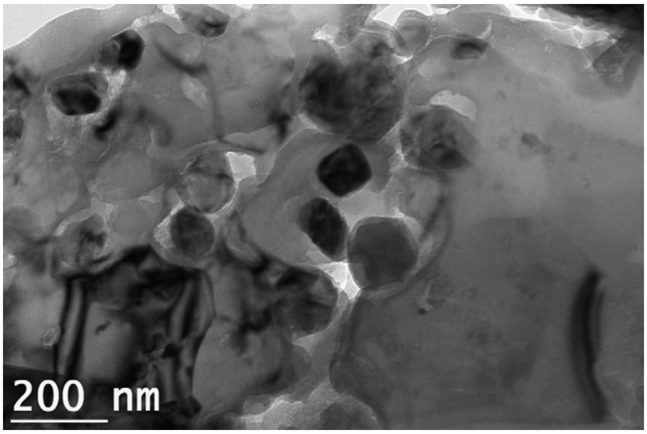

Fig. 4. TEM bright-field image showing the distribution of TiO_2 particles within the grain interior as well as along the grain boundaries of as-sintered AA 6061-10 wt.% TiO_2 composite after 40 h.

of oxides were expected as a result of reaction from surrounding at elevated temperature. The phase evaluation obtained from XRD analysis of AA 6061-10 wt.% TiO_2 composite after sintering is given in Table 1. The crystallite size of α-Al, TiO_2 and Al_2O_3 was measured using XRD peak profile. Crystallite size of α-Al phase after sintering showed a decreasing value from very CG to UFG with milling time due to grain refinement. The increase in milling time pinned the grain growth during sintering. The crystallite size of TiO_2 ceramic phase also showed a decreasing trend to some extend with milling time. However, almost equal crystallite size of Al_2O_3 due to oxidation was observed in all samples. The detailed TEM analysis was carried out for AA 6061-10 wt.% TiO_2 sintered composite after 40 h, which are shown in Figs. 3–5.The grain size distribution was measured by several TEM micrographs (Fig. 3) in which 300 grains were counted. The grain size measured from TEM for 40 h product was about 298 nm which was good agreement with XRD results, and the continuous ring pattern from selected area diffraction also revealed that α-Al matrix grains were in ultra fine level (inset of Fig. 3). The grain size of matrix powder reported elsewhere [13] was 48 nm after 40 h of milling. The increased grain size of α-Al matrix was nearly 5 times after sintering. This was due to severe grain growth occurred, but in ultra fine level. A large number of nano-sized TiO_2 particles were uniformly dispersed in an UFG α-

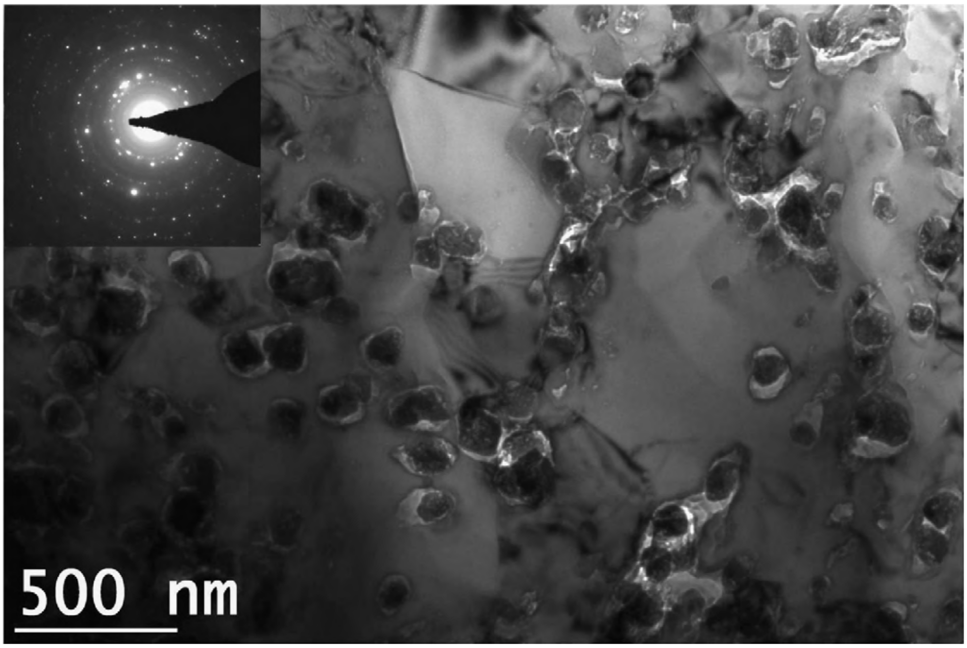

Fig. 3. Bright field image of as-sintered AA 6061-10 wt.% TiO_2 composite after 40 h MA showing the nanometer-size TiO_2 particles embedded in the α-Al matrix. Inset shows the corresponding SAD ring pattern indicating ultra fine crystalline nature.

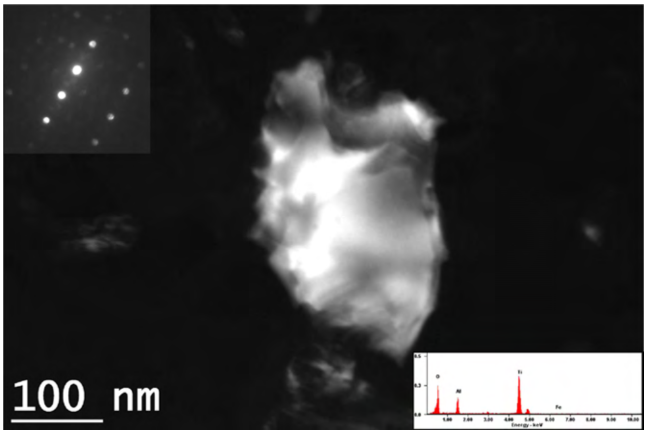

Fig. 5. TEM dark-field image showing a nearly equiaxed TiO_2 particle in an AA 6061-10 wt.% TiO_2 sintered composite. Inset of upper left showing the SAD pattern in [1 0 1] zone axis. Inset of bottom right showing the corresponding EDAX.

Al matrix (Fig. 3). The TiO_2 particles were found within the grain interior as well as along the grain boundaries of the α-Al matrix (Fig. 4). The TiO_2 particles have equiaxed shape (Fig. 5) which was identified by the use of electron diffraction as shown in inset (upper left) of Fig. 5. In addition, the TiO_2 particles were also confirmed by the EDS analysis with TEM as shown in inset (bottom right) of Fig. 5.

3.2. Microstructure and mechanical properties

The microstructure of sintered specimens of 1, 5 and 40 h composite were observed and presented here using SEM/BSEI as shown in Fig. 6. It was observed that severe clustering of TiO_2 particles occurred in the case of 1 h sintered composite (Fig. 6(a) and (b)) and the same was represented by single arrow. Almost uniformly dispersed TiO_2 particles with slight amount of clustering were observed in 5 h sintered composite (Fig. 6(c) and (d)). This was expected due to grain refinement. Fig. 6(f) shows a large number of fine TiO_2 particles were uniformly dispersed in α-Al matrix in the case of 40 h milling. The uniform dispersion of TiO_2 particles was represented by double arrow in Fig. 6. Also, very bright oxide particles (Al_2O_3) (represented by rectangles) were observed in all composite.

To evaluate the mechanical properties of the sintered composites with milling time, hardness was measured. The results of percentage theoretical density, volume fraction of Al_2O_3 and TiO_2 particles and their mechanical properties after sintering with milling time are shown in Table 2. The volume fraction of second phase particles was quantitatively measured using several SEM/BSEI images. The measured theoretical density of 1 and 40 h

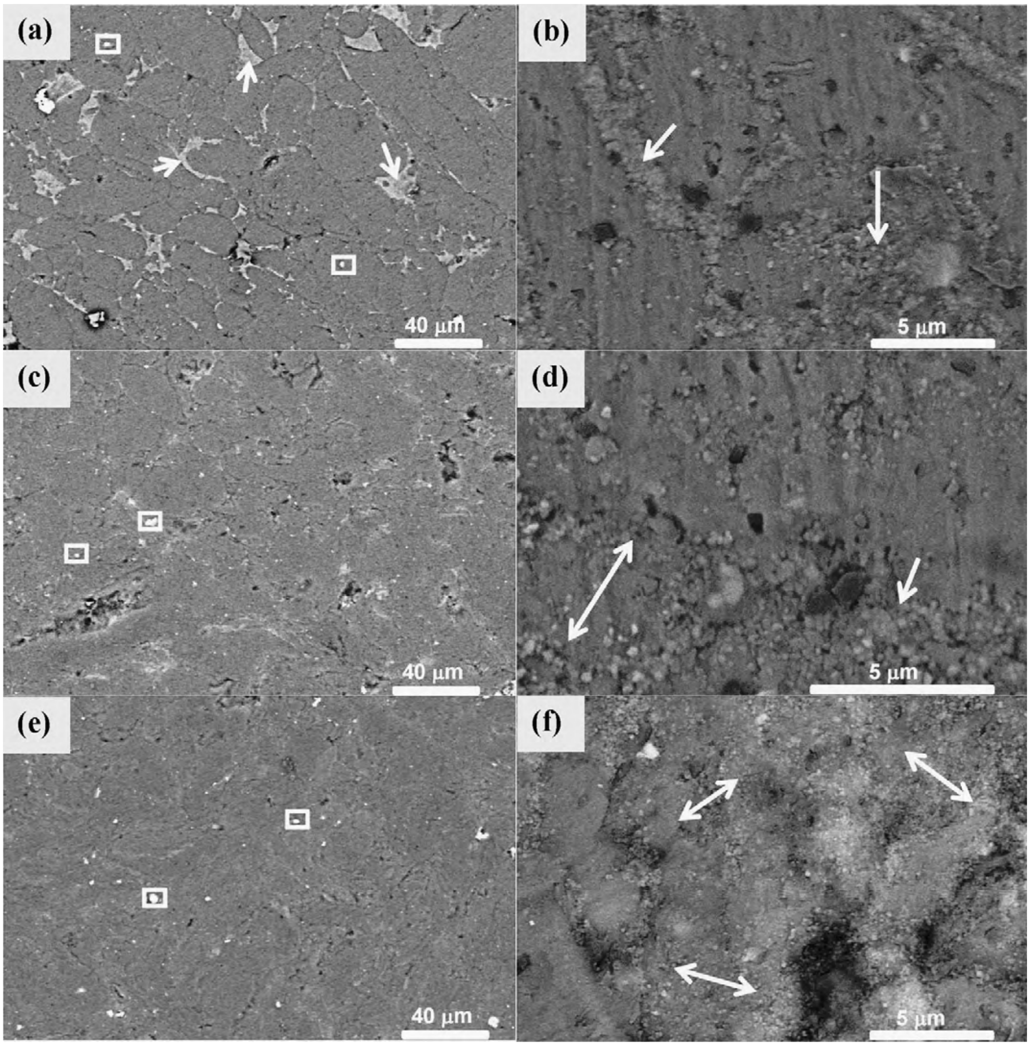

Fig. 6. SEM/BSEI of AA 6061-10 wt.% TiO_2 sintered composite. Left side (a), (c) and (e) shows after 1 h, 5 h and 40 h. Right side (b), (d) and (f) shows magnified view of corresponding composites. *Note*: single arrow represents TiO_2 clusters, double arrow represents distribution of TiO_2 particles and rectangle represents oxide particles.

sintered composite was found to be close to 93% and 82% respectively which meant the theoretical density was decreased with milling time during the same compaction pressure (350 MPa) and sintering time. This can be attributed to grain refinement and its subsequent strengthening mechanisms. Further, this may be due to non-readjustment of particles and pores during compaction because particles are in highly work hardened state after 40 h milling. The highly strain hardened powders, greater than 5 h of milling, decreased the theoretical density of the sintered composite because it exhibited high specific surface energy. The high specific surface energy of FG and UFG composite was expected to enhance the interparticle friction effects; which decreased the density as compared to CG composite. It may be noted that the theoretical density was calculated presuming that the sintered composites consists of α-Al, Al_2O_3 and TiO_2 ternary phases. It was noted that the hardness of 1 h sintered composite was around 245 MPa which was very low value since the hardness of 6061 Al alloy sintered at N_2 atmosphere was 440 MPa as reported [28]. This may be attributed to the formation of TiO_2 clusters (Fig. 6(b)) in the composites as explained elsewhere [13]. However, the hardness value was increased steadily with milling time due to grain refinement. The yield strength (YS), σ_y was obtained from the hardness measurements using the empirical relation $Hv = 3\sigma_y$. As expected, the YS was increased with milling time due to grain refinement and its subsequent strengthening mechanisms. The UFG composite led to YS over 1000 MPa as compared to the very CG composite of 1 h (245 MPa). This fact suggests that the UFG composite is very advantageous for improving matrix strength, so that it would be suitable for use in structural applications.

Young's modulus of particulate reinforced composites can be well predicted from the Halpin-Tsai equation as reported recently by Hsu et al. [29]:

$$E_c = \frac{E_m(1+\eta q V)}{E_p(1-qV)} \tag{1}$$

where,

$$q = \frac{(E_p/E_m)-1}{(E_p/E_m)+\eta} \tag{2}$$

E_c, E_m and E_p are Young's moduli of the composite, matrix, and particles respectively, η is an adjustable parameter, and V is the volume fraction of the second phase particles. E_c and V are calculated based on rule of mixtures. For AA 6061-10 wt.% TiO_2 composites, E_m = 70 GPa, $(E_p)_{TiO_2} = 282.76$ GPa, $(E_p)_{Al_2O_3} = 343.83$ GPa [19]. The predicted Young's modulus increased significantly with milling time.

3.3. Strengthening mechanisms

To explain the deformation behavior, a detailed analysis based on the dislocation models is necessary to investigate the mechanisms governing cold deformation. The probable strengthening mechanisms to the overall strength, i.e. solid solution, grain boundary, dislocation, precipitation and dispersion strengthening were estimated using well-established expressions available in the literatures.

The solid solution strengthening increment ($\Delta\sigma_{ss}$), due to concentration of major solute atoms of Mg, Mn, Cu, Zn, Si from AA 6061 composition is determined by [30]

$$\Delta\sigma_{ss} = AC_o^{2/3} \tag{3}$$

where A is the constant and C_o is the concentration of the solute in weight percent. The value of A for Mg, Mn, Cu, Zn, Si are 20.481, 15.772, 12.431, 3.085 [30], 11.08 [31] respectively. From Eq. (3), the total contribution to strengthening due to solid solution was found to be 39.3 MPa (Table 3).

The contribution from grain boundary strengthening can be calculated from the Hall-Petch equation as,

$$\sigma_{gs} = \sigma_0 + kt^{-1/2} \tag{4}$$

where t is the grain size of α-Al matrix, and σ_0 = 13 MPa and k = 74 MPa μm$^{1/2}$ for pure Al [29]. It was observed from Table 3 that the grain boundary strengthening of 40 h UFG sintered composite was considerably high by a factor of 2.3 times higher than 1 h CG sintered composite.

The increase in strength due to forest dislocation can be estimated by

$$\sigma_{dis} = \alpha MGb\rho^{1/2} \tag{5}$$

where α is a constant of the order of 0.3, M is the Taylor factor (M = 3 for FCC material), ρ_{dis} is the dislocation density [32] and can be determined from XRD analysis using the relation [33]:

$$\rho_D = 2\sqrt{3}\,\frac{\langle\varepsilon_{r.m.s.}\rangle}{tb} \tag{6}$$

where $\langle\varepsilon_{r.m.s.}\rangle$ is RMS lattice strain which is determined as:

$$\langle\varepsilon_{r.m.s}\rangle = \left(\frac{2}{\pi}\right)^{1/2}\left(\frac{\Delta d}{d_{0(hkl)}}\right) \tag{7}$$

$\Delta d = d_{(hkl)} - d_{0(hkl)}$, where $d_{(hkl)}$ and $d_{0(hkl)}$ are the calculated and observed interplanar spacing, t is the crystallite size in 'm' and b is the burgers vector of dislocation in 'm' which is equal to $a/\sqrt{2}$ for the FCC structure, a is lattice parameter in 'm'. The actual lattice parameter was obtained as described by Cullity [27], by constructing the linear plot between the calculated lattice parameter for each Bragg's angle and the corresponding value of $\cos^2\theta/\sin\theta$. The increase in strength by dislocation density of 40 h UFG sintered composite was about 2.77 times higher than 1 h CG sintered composite (Table 3).

Since the sintering was carried out in mechanical pusher furnace and Al is very easy to oxidize, Al_2O_3 phase as a fine precipitate was expected to form during sintering. Therefore, the increase in strength due to fine oxide particles was calculated using [31]:

$$\sigma_{pt} = \frac{2Gb}{\lambda} \tag{8}$$

where G = 26 GPa) and b = 0.286 nm) are shear modulus and burger's vector of the dislocation. λ referring to the interparticle spacing of the dispersed Al_2O_3 particles were calculated individually using the equation below [29]:

$$\lambda = \left[\sqrt{\frac{\pi}{V}} - 2\right]\left(\sqrt{\frac{2}{\sqrt{3}}}\right) r \tag{9}$$

where r is the radius of the particle (Al_2O_3) and refers to half of the crystallite, and assuming the particles are spherical, measured from XRD peak profile (Table 3).

The associated Orowan strengthening due to fine dispersed TiO_2 particles was determined using [29]

$$\sigma_{disper} = \frac{0.81MGb}{2\pi(1-\upsilon)^{1/2}\lambda}\ln\left[2\sqrt{\frac{2}{3}}\frac{r}{r_0}\right] \tag{10}$$

where υ = 0.345 is Poisson's ratio, and $r_0 = 4b$ is the dislocation core radius.

The total strength expected due to the combination of these various strengthening mechanism can be expressed according to superposition laws [32]

$$\sigma_{tot} = \sigma_{gs} + \left[\sigma_{gs}^n + \sigma_{dis}^n + \sigma_{pt}^n + \sigma_{disper}^n\right]^{1/n} \tag{11}$$

where n can vary between 1 (linear superposition) and 2 (Pythagorean superposition). Based upon the microstructural

Table 2
Density, volume fraction of Al_2O_3 ($V_{Al_2O_3}$), TiO_2 (V_{TiO_2}) and mechanical properties of sintered perform.

Milling time, h	Theoretical density, %	Calculated Al_2O_3	Calculated TiO_2	Hardness ($Hv_{1.0}$), MPa	Empirical yield stress (σ_y), MPa	Empirical modulus (E), GPa
01	92.9232	0.03936	0.07283	245.3680	81.7893	80.8454
05	89.5318	0.04715	0.07472	520.3698	173.4566	81.8946
10	86.1471	0.04871	0.07591	774.3698	258.1233	82.2444
20	83.0671	0.05167	0.07751	846.3298	282.1099	82.7906
30	81.7202	0.05221	0.07625	940.3690	313.4563	82.7551
40	81.9371	0.05429	0.07818	1010.3570	336.7857	83.1890

parameters listed in Tables 1 and 2, the contributions of various strengthening such as solid solution, grain size, dislocation, precipitate, dispersoid strengthening to YS are calculated and the same is reported in Table 3. The calculated strength value is almost close to the experimental value when n is equal to 2. It is clearly observed from Table 3 that the grain size and dislocation strengthening are the dominant mechanisms on YS in the present composites in as-sintered condition. The reasons are: as the grains were refined from CG to UFG, the dislocation pile up around the GBs was increased which accumulated more amount of stress concentration at the GBs. As a consequence, a high applied stress is required to promote slip transmission across GBs [29]. Also, a smaller grain size decreased the difference of flow resistance between the GB and interior, which in turn reduced the work hardening [34]. Hence, FG and UFG composites (20, 30 and 40 h (Table 3)) would try to exhibit poor strain hardening during cold-upsetting but yield high strength. This higher yield strength makes it suitable for structural applications.

3.4. Cold workability behavior

The cold upsetting tests were done on sintered composites and the dimensional changes before and after deformation were recorded. Since the material under consideration is porous, the various cold-upsetting parameters under triaxial stress condition are determined with the application of the following expressions [24]:

$$\text{True axial strain}, \varepsilon_z = \ln\left(\frac{h_0}{h_f}\right) \tag{12}$$

$$\text{True hoop strain}, \varepsilon_\theta = \ln\left(\frac{2D_B^2 + D_C^2}{3D_0^2}\right) \tag{13}$$

$$\text{True axial stress}, \sigma_z = \frac{\text{load}}{\text{contact surface area}} \tag{14}$$

$$\text{True hoop stress}, \sigma_\theta = \left(\frac{2\alpha + R^2}{2 - R^2 + 2R^2\alpha}\right)\sigma_z \tag{15}$$

where α is plastic increment ratio which is equal to $(d\varepsilon_\theta/d\varepsilon_z)$, $d\varepsilon_\theta$ and $d\varepsilon_z$ are plastic strain increment in hoop and axial direction respectively, R is the relative density and $d\varepsilon = \varepsilon_i - \varepsilon_{i-1}$. It is assumed that the consecutive compressive/upsetting loads were specified as $1, 2, 3, \ldots, (i-1), i$.

$$\text{True mean or hydrostatic stress}, \sigma_m = \frac{(\sigma_z + \sigma_\theta + \sigma_r)}{3} \tag{16}$$

where σ_r is true radial stress. Since $\sigma_r = \sigma_\theta$ for cylindrical axisymmetric upsetting, then Eq. (16) becomes as follows:

$$\sigma_m = \frac{(\sigma_z + 2\sigma_\theta)}{3} \tag{17}$$

The true effective stress (σ_{eff}) can be determined from the following expression in terms of cylindrical coordinates as explained elsewhere [23]:

$$\sigma_{eff} = \frac{\sigma_z^2 + \sigma_\theta^2 + \sigma_r^2 - R^2(\sigma_z\sigma_\theta + \sigma_\theta\sigma_r + \sigma_z\sigma_r)}{2R^2 - 1} \tag{18}$$

Since $\sigma_r = \sigma_\theta$ Eq. (18) becomes:

$$\sigma_{eff} = \left(\frac{[\sigma_z^2 + 2\sigma_\theta^2 - R^2(\sigma_\theta^2 + 2\sigma_z\sigma_\theta)]}{2R^2 - 1}\right)^{1/2} \tag{19}$$

The cold workability behavior can be investigated by introducing a formability parameter called formability stress index (β_σ) using the relation [24]

$$\beta_\sigma = \frac{3\sigma_m}{\sigma_{eff}} \tag{20}$$

The result of true effective stress with the true axial strain for different milling time is shown in Fig. 7. It is of interest, however, to note that the UFG composite showed a greater strength compared to the CG composite. In fact, the dissociation of trapped lattice dislocations is expected to be more in UFG composite consequently high amount of internal stresses built up in the grain boundaries (GB), which increased the strength. The 1 h milled very CG composite exhibited low effective stress because of higher grain size. This can be attributed to fine reinforcement (TiO_2) clusters played more on the matrix during the initial or shorter milled product as explained elsewhere [13,14]. The CG 5 h composite exhibited substantial amount of the true axial strain before fracture. This may be due to the almost uniform distribution of TiO_2 particles in α-Al matrix. However, the strength is better than 1 h milled composite and lower than 10 h composite. The incremental compressive ductility increased from 11.02% (01 h) to 23.03% (5 h). This meant that 5 h milled composite exhibited good workability. This

Table 3
Calculated contribution of solid solution strengthening (σ_{ss}), Orowan strengthening (σ_{disper}), grain size strengthening (σ_{gs}), dislocation strengthening (σ_{dis}) and precipitates strengthening (σ_{pt}) to the empirical yield strength (σ_y) of sintered AA 6061-10 wt.% TiO_2 composites.

Milling time, h	σ_{ss}, MPa	σ_{disper}, MPa	σ_{gs}, MPa	σ_{dis}, MPa	σ_{pt}, MPa	σ_{Total}, MPa		σ_y, MPa
						$n = 1$	$n = 2$	
1	39.2968	134.1959	58.4786	48.3233	117.2758	397.5706	232.9901	81.7893
5	39.2968	151.4258	83.1643	48.7764	119.8478	442.5113	255.1411	173.4566
10	39.2968	154.9510	100.2512	73.1523	124.2062	491.8577	273.4733	258.1233
20	39.2968	163.0210	121.0159	103.9765	127.9747	555.2852	300.8487	282.1099
30	39.2968	164.6013	134.2261	129.6732	126.6844	594.4820	318.5357	313.4563
40	39.2968	170.4613	136.9561	133.4917	130.6406	610.8468	326.8748	336.7857

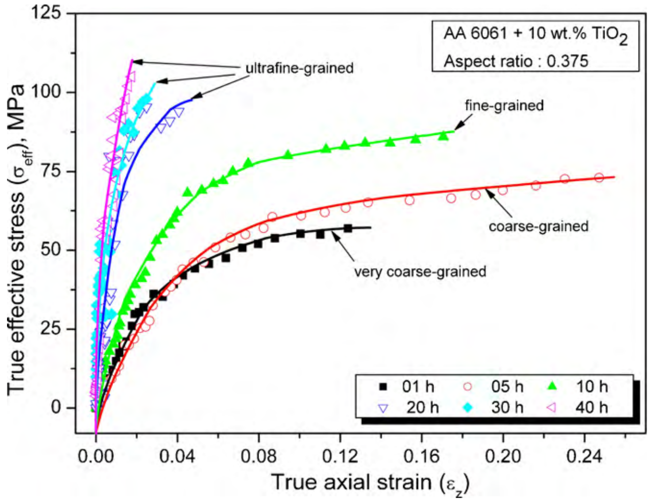

Fig. 7. Variation of true effective stress with true axial strain as a function of milling time for AA 6061-10 wt.% TiO_2 sintered composites.

was attributed to a good homogeneous dispersion and embedding of TiO_2 particles on the α-Al matrix and grain refinement. However, the FG or UFG samples, 20, 30 and 40 h showed a very high true effective stress, limited the true axial strain and the decrease in incremental compressive ductility which were in the order of 3.19%, 2.29% and 1.59% respectively, due to increased YS as a result of grain refinement. The value of true effective stress of UFG sintered composite showed at least about two times higher than very CG composite. It was concluded that, as the grains were refined from very CG to UFG in as-sintered condition after MA for different milling times, the samples exhibited high effective stress, i.e. high compressive YS (Table 2) because of grain refinement. This may be further due to uniform distribution of TiO_2 particles in α-Al matrix and increased dislocation density of individual grains after milling. As provided in Table 2, the volume fraction of Al_2O_3 oxide particles increased with increasing milling time or decreasing grain size due to the reason that very ultra fine powders possess greater surface energy. The poor compression ductility was also experienced by Shanmugasundaram et al. [32] while studying the Al–4 wt.%Cu produced by MA and vacuum hot pressing.

Fig. 8(a) and (b) shows the variation of the true hydrostatic stress (σ_m) and formability stress index (β_σ) with true axial strain of AA 6061-10 wt.% TiO_2 sintered composite milled for different time (1, 5, 10, 20, 30 and 40 h). As the grains were refined from coarser to ultra fine level, the specific surface area of the material increased which resulted in a large number of grain boundaries [35]. On the other hand, the particle mass to surface area ratio decreased during grain refinement which enhanced the interparticle friction effects. This interparticle friction effect decreased the density of the composite [35]. When the grain size was reduced to ultra fine, a large number of fine pores were developed as observed in the SEM images (Fig. 6). Whereas in the case of lower milling time, irregular shaped pores were found in the composite and they were not uniformly distributed. As shown in Fig. 8(a), the lower milling time or coarse polycrystalline composite exhibited greater deformation than that of ultra fine polycrystalline composite. In UFG composite, the pores were larger in number even though they were uniformly distributed (Fig. 6), and this made the compact not to obtain higher densification. This meant interparticle friction effects dominated during grain refinement which increased a very high value of hydrostatic stress with no deformation for UFG composite. It was observed that the true hydrostatic stress (Fig. 8(a)) increased slightly between 1 and 5 h composite. The UFG composites (20, 30 and 40 h) exhibited a high value of hydrostatic stress with no deformation. This might be due to the domination of interparticle friction effects and the contribution of various strengthening mechanisms as explained in the previous section. It was interesting to note that the formability stress index (Fig. 8(b)) increased with true axial strain from 1 to 5 h sintered composite due to grain refinement, homogeneous dispersion of TiO_2 particles compared to 1 h and retaining considerable amount of ductility up to 5 h (Table 2). A better workability could be obtained in α-Al metal matrix composite by adding high percentage of fine reinforcement (here 10 wt.% TiO_2) at 5 h of milling via MA route. In general, a fine reinforcement would make clustering in the matrix beyond to critical value, i.e. matrix-to-reinforcement ratio exceeds one (here ≈45); which was eliminated via MA [13,14]. This 5 h composite showed a better performance as far as workability concerned. This was attributed to a good homogeneous dispersion and grain refinement as explained above. Therefore, 5 h milled products may be used to produce light weight metal matrix composite particularly in automotive applications. On the other hand, the formability stress index was decreased with true axial strain for higher milling time (i.e. beyond 5 h). In these cases, the deformation strain is very less. Further, this might increase YS as a result of grain refinement and contribution of various strengthening mechanisms. Among the developed strengthening mechanisms the grain size and the dislocation strengthening mechanism may reduce the formability stress index of the composites beyond 5 h of milling.

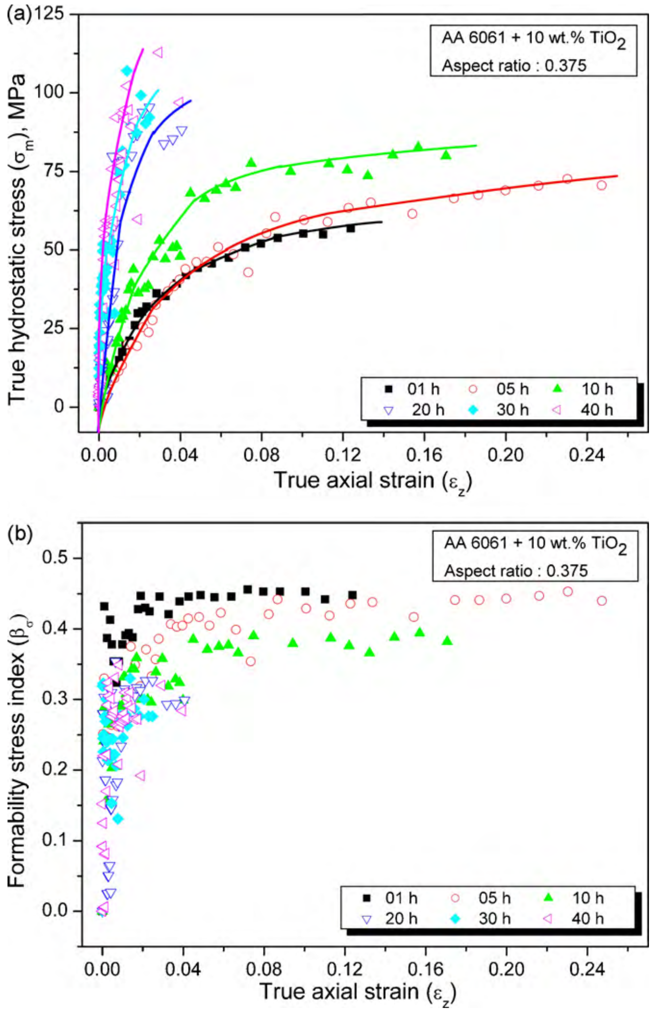

Fig. 8. Variation of (a) true hydrostatic stress with true axial strain (b) formability stress index with true axial strain, as a function of milling time for AA 6061-10 wt.% TiO_2 sintered composites.

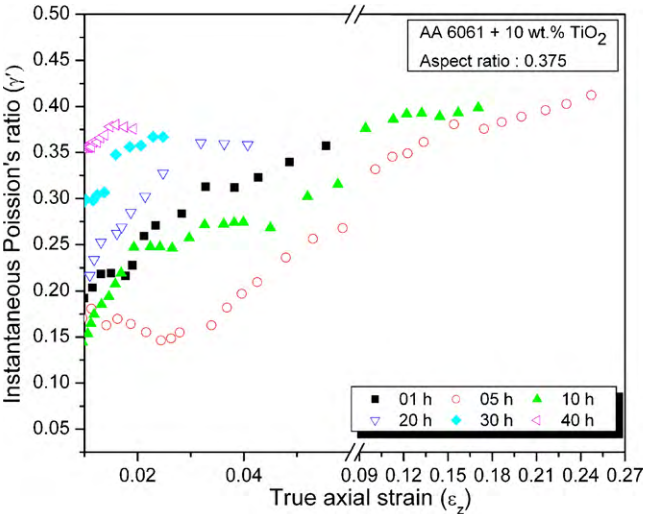

Fig. 9. Variation of instantaneous Poisson's ratio with true axial strain as a function of milling time for AA 6061-10 wt.% TiO_2 sintered composites.

To study the plastic deformation capacity and plastic strain levels of the material or composite, instantaneous new Poisson's ratio (ν_i) was introduced [24]. Poisson's ratio (ν), as normally defined for uniform simple compression, is the ratio of lateral extension to longitudinal compression. Here, as the cylindrical sintered preforms were subjected to compress in one direction (longitudinal), it tends to expand in the other two directions (i.e. radial and hoop). This phenomenon is called Poisson's effect [36]. To study the Poisson effect, the instantaneous new Poisson's ratio (ν_i) was introduced here; which could be calculated as below [24]:

$$\nu_i = \frac{\varepsilon_\theta}{2\varepsilon_z} \tag{21}$$

The variation of instantaneous Poisson's ratio with the true axial strain as a function of milling time is shown in Fig. 9. It was observed that at lower true axial strain value the instantaneous Poisson's ratio increased drastically as the milling time increases, i.e. during grain refinement, but limited the deformation capacity during upsetting or further deformation. In general, a higher value of Poisson's ratio reduces the extent of plastic zone and plastic strain level [36]. For 5 h composite, the instantaneous Poisson's ratio vale was found to be high at higher strain value. This meant more plastic deformation has taken place. The reason for more plastic deformation is stated above. Hence, the proposed instantaneous new Poisson's ratio could also be used to measure the plastic deformation capacity of the material.

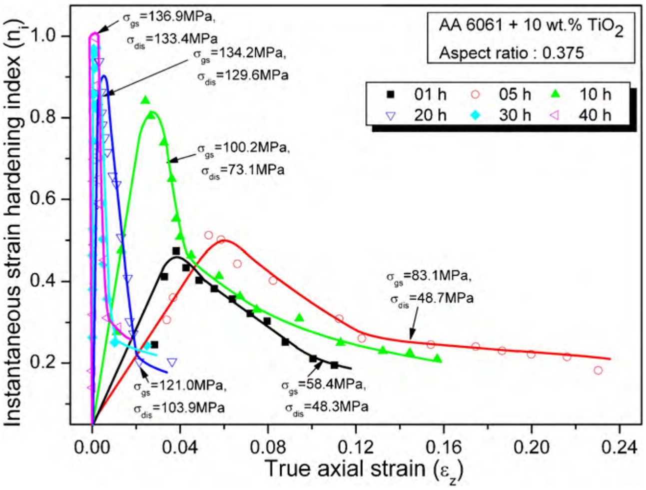

Fig. 10. Variation of instantaneous strain hardening index with true axial strain as a function of milling time for AA 6061-10 wt.% TiO_2 sintered composites.

3.5. *Instantaneous strain hardening behavior*

To correlate the strengthening mechanism (developed dislocation models) with strain hardening behavior, a term called instantaneous strain hardening index (n_i) was introduced and explained by the equation as [24]

$$n_i = \frac{\ln((\sigma_{eff})_i/(\sigma_{eff})_{i-1})}{\ln((\varepsilon_z)_i/(\varepsilon_z)_{i-1})} \tag{22}$$

Fig. 10 shows the instantaneous strain hardening index with axial strain of cold deformed composites to different milling time. As the grains were refined from very CG to UFG the maximum instantaneous strain hardening index value increased steeply during the early stage which corresponds to YS. Also, it is clearly seen from Fig. 10 that the CG sintered composite (5 h) exhibited larger amount of geometry work hardening and considerable matrix work hardening than very CG composite (1 h). This might be due to homogeneous dispersion and embedding of TiO_2 particles on the α-Al matrix and as well grain refinement. Further milling time (i.e. greater than 5 h), the amount of both geometry work hardening (related to relative density) and the matrix work hardening decreased drastically. The UFG especially in 40 h composite exhibited poor work hardening. This was expected that the plastic instability in the form of localized deformation was enhanced due to the various contribution of strengthening mechanisms. Among the developed strengthening mechanisms the grain size and dislocation strengthening mechanism diminished the strain hardening capacity of the composites (see Table 3 and Fig. 10) because it increased the resistance to the dislocation movement, i.e. increased the strong barriers in terms of pores to the dislocation movement. This would decrease the ductility of the refined (FG and UFG) composites. Hence, the stress required to deform the materials becomes higher during cold-upsetting.

3.6. *Fracture limit strain and percent cold workability*

The most obvious fracture limit strain is based on assuming that void growth attains a critical value at which the load-carrying capacity of the material vanishes [37]. As the cold deformation was carried out at room temperature, the percentage of cold workability (%CW) under incremental load could be calculated as:

$$\%CW = \frac{100(A - A_0)}{A_0} \tag{23}$$

where A_0 and A were initial and final cross-sectional area of the specimen.

The relation between fracture limit strain and percentage of cold work done on the composites to different milling time is shown in Fig. 11. It was clearly observed that 5 h milled composite exhibited better workability due to grain refinement and homogeneous dispersion with sustaining considerable ductility. In general, during cold deformation, the grain shape changes and the grains become aligned in the deformation direction. The grain shape changes and the grain orientation after cold deformation for 5 h sintered composite in perpendicular to the axial, the hoop and radial direction is shown in Fig. 12. It was clearly observed that randomly oriented grains were observed in perpendicular to axial direction, whereas very long elongated and aligned grain boundaries were observed both in perpendicular to hoop and radial direction. This resulted in a heavy plastic deformation occurring in the case of 5 h sintered composite. But this was limited for other composites.

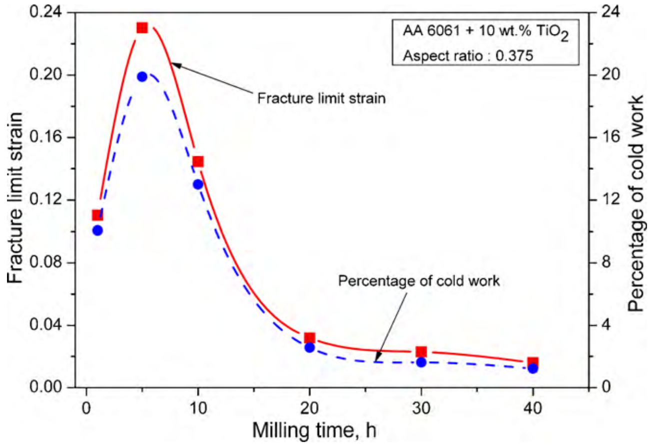

Fig. 11. Variation of fracture limit strain and percentage of cold work with true axial strain as a function of milling time for AA 6061-10 wt.% TiO_2 sintered composites.

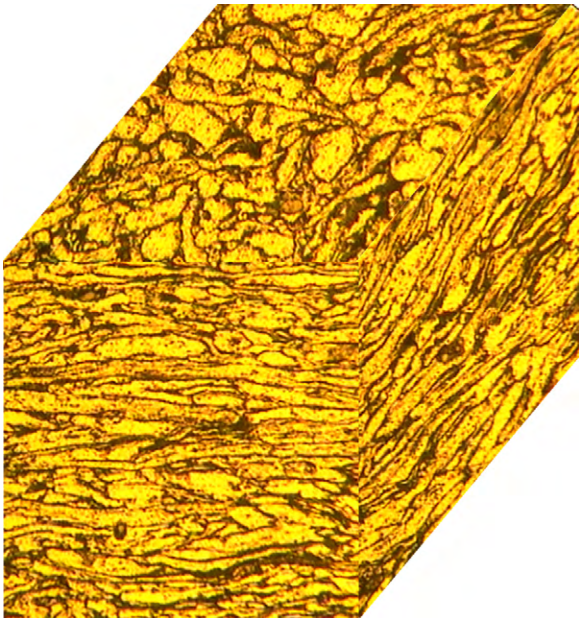

Fig. 12. 3D microstructure of AA 6061-10 wt.% TiO_2 composite for 5 h specimen after cold deformation in perpendicular to axial (top), hoop (front) and radial (right)—magnification 200×.

4. Conclusions

This study examined the different strengthening mechanisms in AA 6061-10 wt.% TiO_2 sintered composites for different milling times (1, 5, 10, 20, 30 and 40 h) i.e. during grain refinement by MA using simple models based on literatures; which addressed the effects from solid solution, grain size, precipitate, dislocation and dispersion strengthening. The microstructure, mechanical properties, cold workability and strain hardening behavior under triaxial stress state condition were investigated by correlating the various strengthening mechanisms. The basic conclusions are listed in the following:

- The 5 h sintered sample showed considerable strength of greater than 500 MPa with large plastic strain of 23% at room temperature and this meant that a good workability was obtained on this composite.
- Further this composite exhibited a high percent cold work of around 20% compared to other composites.
- The 40 h sintered composite showed a very high strength of greater than 1000 MPa. This can be attributed to the reduction of grain size from very CG level to UFG level of α-Al matrix, contribution of various strengthening mechanisms and complete embedding of nanometer-sized TiO_2 particles on α-Al matrix (see TEM microstructure of Figs. 3–5).
- As the grain size is reduced from CG (greater than 5 h) to UFG level, the cold workability and the corresponding strain hardening behavior were drastically decreased. This was expected due to the domination of interparticle friction effects, grain size and dislocation strengthening mechanism.
- The proposed instantaneous new Poisson's ratio and the instantaneous strain hardening index were used to study the extent of plastic zone and strain levels of the composite or any bulk material during compressive deformation.

Acknowledgment

The authors wish to express their gratitude to the General Manager, HAPP for permitting to utilizing the facilities of Powder Metallurgy Shop, Heavy Alloy Penetrator Project (HAPP), Tiruchirappalli, Tamil Nadu, India.

References

[1] J. Fecht, E. Hellstern, Z. Fu, W.L. Johnson, Metall. Mater. Trans. A 21A (1990) 2333–3337.
[2] R.Z. Valiev, R.K. Islamagaliev, I.V. Alexandrov, Prog. Mater. Sci. 45 (2000) 103–189.
[3] Y.T. Zhu, G. Jiang, J.Y. Huang, T.C. Lowe, Metall. Mater. Trans. A 32A (2001) 1559–1562.
[4] S.H. Wang, P.W. Kao, C.P. Chang, Scr. Mater. 40 (3) (1999) 289–295.
[5] D. Srinivasan, K. Chattopadhyay, Mater. Sci. Eng., A 255 (1–2) (1998) 107–116.
[6] E.J. Lavernia, J.D. Ayers, T.S. Srivatsan, Int. Mater. Rev. 37 (1) (1992) 1–44.
[7] J.B. Fogagnolo, E.M. Ruiz-Navas, M.H. Robert, J.M. Torralba, Scr. Mater. 47 (4) (2002) 243–248.
[8] J.B. Fogagnolo, F. Velasco, M.H. Robert, J.M. Torralba, Mater. Sci. Eng., A 342 (1–2) (2003) 131–143.
[9] L.E.G. Cambronero, E. Sanchez, J.M. Ruiz-Roman, J.M. Ruiz-Prieto, J. Mater. Process. Technol. 143–144 (2003) 378–383.
[10] J.S. Benjamim, T.E. Volin, Metall. Trans. A 5 (1974) 1929–1934.
[11] C. Suryanarayana, Prog. Mater. Sci. 46 (1–2) (2001) 1–184.
[12] A. Slipenyuk, V. Kuprin, Yu. Milman, V. Goncharuk, J. Eckert, Acta Mater. 54 (1) (2006) 157–166.
[13] S. Sivasankarana, K. Sivaprasad, R. Narayanasamy, V.K. Iyer, J. Alloys Compd. 491 (1–2) (2010) 712–721.
[14] S. Sivasankarana, K. Sivaprasad, R. Narayanasamy, V.K. Iyer, Powder Technol. 201 (2010) 70–82.
[15] N. Afrin, D.L. Chen, X. Cao, M. Jahazi, Scr. Mater. 57 (2007) 1004–1007.
[16] Y.G. Ko, D.H. Shin, K.T. Park, C.S. Lee, Scr. Mater. 54 (2006) 1785–1789.
[17] X.H. Chen, L. Lu, Scr. Mater. 57 (2) (2007) 133–136.
[18] Y.M. Wang, E. Ma, Mater. Sci. Eng., A 375–377 (2004) 46–52.
[19] M.L. Young, J. DeFouw, J.D. Almer, D.C. Dunand, Acta Mater. 55 (2007) 3467–3478.
[20] A.A. Salem, S.R. Kalidindi, R.D. Doherty, Acta Mater. 51 (2003) 4225–4237.
[21] H. Petrik, S. Stupkiewicz, R. Kuziak, J. Mater. Process. Technol. 204 (2008) 255–263.
[22] R. Narayanasamy, T. Ramesh, K.S. Pandey, Mater. Des. 27 (2006) 566–575.
[23] R. Narayanasamy, T. Ramesh, K.S. Pandey, Mater. Des. 29 (5) (2008) 1011–1026.
[24] R. Narayanasamy, V. Anandakrishnan, Mater. Des. 29 (8) (2008) 1582–1599.
[25] R. Narayanasamy, T. Ramesh, K.S. Pandey, Mater. Des. 29 (4) (2008) 891–903.
[26] G.K. Williamson, W.H. Hall, Acta Metall. 1 (1) (1953) 22–31.
[27] B.D. Cullity, Elements of X-ray diffraction, second ed., Addision Wesley, London, UK, 1978.
[28] N. Showaiter, M. Youseffi, Mater. Des. 29 (2008) 752–762.
[29] C.J. Hsu, C.Y. Chang, P.W. Kao, N.J. Ho, C.P. Chang, Acta Mater. 54 (2006) 5241–5249.
[30] M. Dixit, R.S. Mishra, K.S. Sankaran, Mater. Sci. Eng., A 478 (2008) 163–172.
[31] J.F. Shackelford, W. Alexander, CRC Materials Science and Engineering Hand Book, third ed., 2001.
[32] T. Shanmugasundaram, M. Heilmaier, B.S. Murty, V. Subramanya Sarma, Metall. Mater. Trans. A 40A (2009) 2798–2801.
[33] Y.H. Zhao, H.W. Shang, K. Lu, Acta Mater. 49 (2001) 365–375.
[34] J. Luo, Z. Mei, W. Tian, Z. Wang, Mater. Sci. Eng., A 441 (2006) 282.
[35] Powder Metal Technologies and Application, vol. 7, ASM International, 1998.
[36] H. Gercek, Int. J. Rock Mech. Min. Sci. 244 (1) (2007) 1–13.
[37] A.R. Ragab, Eng. Fract. Mech. 71 (11) (2004) 1515–1534.